Toward Climate Prediction: Interannual Potential Predictability due to an Increase in CO₂ Concentration as Diagnosed from an Ensemble of AO GCM Integrations

JIN-SONG VON STORCH

Max Planck Institute for Meteorology, Hamburg, Germany

ABSTRACT

Predictability studies of the second kind are often carried out to address the potential in predicting atmospheric variables based on knowledge of changes in sea surface temperature (SST). Here a predictability study of the second kind is performed for the coupled atmosphere–ocean system based on knowledge of changes in CO_2 concentration. The focus is on potential predictabilities obtained after imposing a CO_2 forcing over a short time period (i.e., a few years), which are less sensitive to the exact future time evolution of the CO_2 forcing. Potential predictability is measured by the ensemble mean difference resulting from the CO_2 forcing relative to the ensemble spread subjected to the same forcing. The measure is calculated from a 50-member prediction ensemble obtained from an atmosphere–ocean GCM forced by a 3% increase in CO_2 concentration per year and a reference ensemble obtained under a constant CO_2 concentration.

The largest potential predictabilities are found in and over the Southern Ocean. The origin of these predictabilities is a positive feedback involving interactions between the atmosphere and the upper ocean. An increase in the meridional gradient of SST resulting from a large SST increase in the southern subtropics leads to a strengthening of atmospheric circulation, and from that increases in surface zonal wind stress result. The latter enhances the northward Ekman transport over the southern high latitudes, which transports polar water equatorward, whereby maintaining the meridional temperature gradient. Potential predictability is also found in the deep ocean, characterized by the downward propagation of the surface warming within a few years through two "corridors," located at 40°S and 40°N and extending from the near surface to about 3000–3500 m. The warming in the atmosphere and the upper ocean is reduced by half because of this downward heat propagation.

1. Introduction

Weather predictions, as they are performed in various meteorological centers, generally have a lead time of about several days. The short lead time reflects the limit set by the chaotic nature of the system, which initiates *predictability studies of the first kind.* A small uncertainty in the initial condition could make the prediction quickly deviate from the true evolution. Because the external forcing of the climate system changes little during a lead time of several days, weather prediction is traditionally performed under a constant external forcing or a constant boundary condition.

A climate prediction is generally understood as a prediction of some averaged climate variables, for example, January mean temperature, over a longer lead time, for example, several months or even longer. During such a long time period, forcing external to climate can change notably. If the change in the forcing produces systematic responses, one would be able to predict the climate for a given time evolution of forcing, even though the skill of weather prediction is limited. Studies on predictability induced by changing external forcing are known as *predictability studies of the second kind.* Thus far, the focus has been mainly on the seasonal forecast of the atmosphere, and thereby considering the SST anomalies, for example, those resulting from an ENSO event, as the external forcing. A deviation of the SST from its climatological mean value can result in a predictable atmospheric response. This paper extends the predictability study of the second kind for the atmosphere to one for the coupled atmosphere–ocean system. The external forcing considered is that resulting from changes in the CO_2 concentration.

When constraining a real-time prediction by a chang-

Corresponding author address: Jin-Song von Storch, Max Planck Institute for Meteorology, Bundesstrasse 53, Hamburg D-20146, Germany.
E-mail: jin-song.von.storch@zmaw.de

ing external forcing, one encounters the problem that the future evolution of the forcing must be known prior to the prediction. This means that one needs to first predict the SST changes in case of seasonal forecasts, and the future CO_2 changes in the case of climate changes. Often, predictions of the external forcing are highly uncertain. Some of previous studies on seasonal prediction tackle the problem by forcing the prediction model using SST anomalies observed in the past decades (e.g., Rowell 1998; Compo and Sardeshmukh 2004; Tippett et al. 2004; Kumar and Hoerling 1998). In the case for which a response to SST is identified from predictability studies using past SST forcing, a prediction based on this forcing–response relation would have notable prediction skill, given the sign of the emergence of SST anomalies.

It seems that studying predictability of the second kind is possible, even when predicting the exact future evolution of external forcing is still unresolved. This is particularly true for short lead times. To formulate this in a more formal way, consider the evolution of the coupled system $\mathbf{x}[\mathbf{F}(t)]$ forced by the time-varying forcing $\mathbf{F}(t)$. Here, $\mathbf{F}(t)$ can be decomposed into a constant term $\mathbf{F}_0$ and a time-varying component $\mathbf{F}'$, which is switched on at time $t_0 = 0$. For a sufficiently small lead time t (after $\mathbf{F}'$ being switched on), the response of $\mathbf{x}$ to $\mathbf{F}'$, $\Delta\mathbf{x} = \mathbf{x}(t) - \mathbf{x}(0)$, can be approximated by the leading term in the Taylor expansion

$$\Delta\mathbf{x} = \left.\frac{\partial\mathbf{x}}{\partial\mathbf{F}}\right|_0 \Delta\mathbf{F}|_0. \qquad (1)$$

The amplitude of the response is determined by $\Delta\mathbf{F}|_0 = \partial\mathbf{F}'/\partial t|_0 t$, that is, by the time rate of change of $\mathbf{F}'$ at $t_0 = 0$; $\partial\mathbf{x}/\partial\mathbf{F}|_0$ is the sensitivity of $\mathbf{x}$ to $\mathbf{F}$ at time t_0. For a multivariate variable $\mathbf{x}$, the structure of the response is described by $\partial\mathbf{x}/\partial\mathbf{F}|_0$. Because $\partial\mathbf{x}/\partial\mathbf{F}|_0$ describes the dependence of $\mathbf{x}$ on $\mathbf{F}$ before $\mathbf{F}$ starts to change, the structure of the response is independent of $\mathbf{F}'$. As long as Eq. (1) is appropriate, the same responses, at least with respect to their structure, will be obtained. Equation (1) is appropriate for small $\Delta\mathbf{F}|_0 = \partial\mathbf{F}'/\partial t|_0 t$, which is generally the case when t is small.

The situation is different for a large t for which Eq. (1) is no longer appropriate. The response has to be determined by time integrating the equations of $\mathbf{x}$ subjected to $\mathbf{F}$. When $\mathbf{x}$ is a nonlinear function of $\mathbf{F}$, the sensitivity $\partial\mathbf{x}/\partial\mathbf{F}$ generally changes during the time integration, depending on the time evolution of $\mathbf{F}'$. Accordingly, the structure of the responses changes with lead time, depending on the time evolution of $\mathbf{F}'$. Predicting $\mathbf{x}$ based on the knowledge of $\mathbf{F}'$ is only possible, when the exact future evolution of $\mathbf{F}'$ is known.

The above consideration is consistent with the view (Zwiers 2002) that simulations of the twenty-first century using different scenarios of future emission change can be considered as forecasts of future climate change, at least for relatively short 1–2 decade periods. This is because climate responses at these lead times, at least their structures, appear not to be very sensitive to the details of the forcing scenario chosen. The view is further confirmed by a recent study (Lee et al. 2006), in which notable prediction skills are found based on the estimated response to historical external forcing.

The present predictability study makes use of the above consideration and concentrates on first responses, that is, responses obtained after the change in CO_2 forcing has been imposed over a *short* lead time, for example, less than one decade. By concentrating on small lead times, the identified predictability, in particular its structure can be considered less sensitive to the exact time evolution of the forcing.

Generally, the potential predictability resulting from an increase in CO_2 concentration is strongly related to studies concerning detection of the climate change signal and climate projections summarized by the Intergovernmental Panel on Climate Change (IPCC) Fourth Assessment Report (AR4). However, both the detection studies (e.g., Hegerl et al. 1996) and the IPCC scenario runs have been focused on large climate responses obtained after forcing a climate model with increasing CO_2 concentration over 1–2 centuries, rather than responses obtained over a short time period of a few years.

When studying first responses, one faces the problem that the signal-to-noise ratio is generally low. This makes the use of ensembles more pressing than in detection and projection studies. The result presented below is based on a 50-member ensemble.

The paper is organized as follows. The method used to identify potential predictability is outlined in section 2. The model and the ensemble experiments are described in section 3. The potential predictability in the atmosphere at the air–sea interface and in the ocean is discussed in sections 4–6. Discussion and conclusions are given in section 7.

2. Method

Predictability studies require a quantitative measure of predictability. Thus far an assortment of different measures has been used. Many of them consider the assessment of predictability to be a stochastic problem and utilize two ensembles to quantify predictability. The ensembles are described in the phase space of the prediction model in which, at any time, the state of one

ensemble member is represented by a point and the states of an ensemble by a cloud of points. The latter defines a probability density function (PDF). One ensemble, hereafter referred to as the prediction ensemble, consists of predicted states at different lead times. The other one, the reference ensemble, consists of the states of a "control" climate obtained under fixed forcing conditions. Normally the shape of the prediction ensemble changes with lead time, whereas the reference ensemble is assumed to have a stationary distribution. The latter is described by the distribution derived from a long single control integration under ergodicity assumption.

In many previous studies, predictability is defined by a measure of the difference between a prediction and the reference PDF. As long as there is a difference, the prediction is considered to have more skill than the prediction obtained by just a randomly chosen state from the reference climate. Predictability is said to be completely lost, when the prediction PDF becomes identical to the reference PDF. The predictability measures used can be classified into two classes.

The first class of measures focuses on the difference in variances (or the spreads) of the two PDFs (Murphy 1988; Shukla 1981). If the spread of the prediction ensemble becomes equal to the spread of some reference ensemble, the predictability is said to be completely lost. For multivariate predictions, Schneider and Griffies (1999) further generalized this class of measures by using entropy based on information theoretical principles. For Gaussian distributions, the resulting measure is related to the ratio of the covariance matrix of the actual PDF to that of the reference PDF. Generally, measures based on variances are used when the mean of the prediction ensemble is the same as the mean of the reference ensemble.

The second class of measures takes the difference in the whole probability distribution, including that in the mean, into account (Anderson and Stern 1996; Kleeman 2002; Tippett et al. 2004). The ensemble mean is important for predictability studies of the second kind, that is, when predictability is assumed to originate from a time-varying forcing. This is particularly true when the external forcing persists with the same sign and even increases its amplitude with time, so that notable changes in the mean are expected as lead time increases. The reference ensemble is defined as the climate obtained under the constant external forcing $\mathbf{F}_0$. As the change $\Delta\mathbf{F}$ becomes increasingly noticeable with increasing lead time, the mean of the prediction ensemble is expected to become increasingly different from that of the reference one. This difference in the mean, which leads to the potential predictability, has to be taken into account by the measure chosen.

If one is interested in detecting the changes in the mean only, predictability measures used by Anderson and Stern (1996) and Tippett et al. (2004), or even a simpler one based on a t test, should be sufficient. However, a large change in the mean does not always imply a high prediction skill. This is because, for a given external forcing, there are generally many different states that are all consistent with the forcing. If a large change in the mean is accompanied by a large uncertainty, it would be difficult to turn the predictability that is identified by the change in the mean only into true prediction skill.

To explicitly take the uncertainty resulting from the ambiguity of forcing into account, the predictability will be measured by a signal-to-noise ratio

$$S_t = \frac{\text{ensemble mean difference}}{\text{ensemble spread}} = \frac{|\bar{x}_{p,t} - \bar{x}_r|}{\hat{\sigma}_{p,t}}, \quad (2)$$

where x is a component of the state $\mathbf{x}$ of the prediction model, the subscripts p and r indicate a quantity of the prediction and reference ensemble, t is the lead time and is the ensemble average. The ensemble mean difference $\bar{x}_{p,t} - \bar{x}_r$ represents the signal resulting from the changing CO_2 forcing for component x at lead time t. The ensemble spread

$$\hat{\sigma}_{p,t} = \overline{(x_{p,t} - \bar{x}_{p,t})^2}^{1/2} \quad (3)$$

quantifies the uncertainty that results from the internal dynamics independent of the CO_2 forcing. A large change in the mean enhances predictability, while a large ensemble spread lowers the predictability.

The usefulness of signal-to-noise ratio has been pointed out by several studies concerning predictabilities induced by SST forcing (Kumar and Hoerling 2000; Sardeshmukh et al. 2000; Compo and Sardeshmukh 2004). In particular, it is found that the signal-to-noise ratio is related to the expected correlation skill of an ensemble mean forecast.

The true value of S (i.e., S obtained from the entire prediction and reference populations) ranges from zero, when there is no gain in predictability resulting from external forcing, to infinite, when the external forcing uniquely determines the state of the prediction model so that the ensemble spread is zero. When working with finite samples of the prediction and reference ensembles, S can be nonzero even when the prediction ensemble has the same mean as the reference ensemble. This situation is assessed by testing the null hypothesis of no change in the mean.

When considering yearly values, as it is the case in

this paper, x_p and x_r are by and large independent. Furthermore, x_p and x_r are, by virtue of the central limit theorem, approximately Gaussian distributed. Thus, when neglecting difference in the variance, x_p and x_r will be independent and identically distributed under the null hypothesis. Under this circumstance,

$$R = \frac{\bar{x}_p - \bar{x}_r}{\hat{\sigma}_{pr}(1/n_p + 1/n_r)^{1/2}} = S \frac{\hat{\sigma}_p}{\hat{\sigma}_{pr}(1/n_p + 1/n_r)^{1/2}} \quad (4)$$

is t distributed with $n_p + n_r - 2$ degrees of freedom, where $\hat{\sigma}_{pr}^2$ is the pooled estimate of the common variance and n_p and n_r are the sizes of the prediction and reference ensemble. In the present case with $n_p = 100$ and $n_r = 50$, $n_p + n_r - 2$ is sufficiently large so that the respective t distribution approaches the standard normal distribution. The critical value S_*, obtained such that the probability for $S > S_*$ under the null hypothesis is 5%, equals $1.96 \times (1/n_p + 1/n_r)^{1/2} = 0.34$. If the observed value of S is larger than S_*, the null hypothesis of no change in the mean is rejected at 5% significance level. In the following, the strength of predictability will be quantified by the values of S that are nonzero at 5% significant level.

Strictly speaking, the assumptions of equal variance and independence (i.e., no serial correlation) are not satisfied. An examination of variances and serial correlations in the model data suggests that nonequal variances and serial correlations can alter the critical value by up to 20% and increases S_* from 0.34 to about 0.4. Thus, care should be taken when interpreting S values of about 0.4.

It is noted that the critical value S_* decreases with increasing sample size and approaches zero as n_p and n_r go to infinite. Thus, a nonzero S will always be statistically significant when sufficiently large ensembles are considered, which is a problem discussed extensively in von Storch and Zwiers (1999). Because of this problem, one should not blindly rely on the result of the statistical test. Instead, physical interpretations of the signals found should also be sought.

In Eq. (2), the signal-to-noise ratio is given in a univariate form. This is done deliberately to cooperate with marginal distribution functions, which is important in the present study. Given a short lead time, the increase in the CO_2 forcing may be so small that only a few components of $\mathbf{x}[\mathbf{F}(t)]$ respond to the increase, while others, in particular the oceanic components, remain essentially unchanged. Such a situation can be described by considering marginal distributions. It is possible that one component responds notably to the changing external forcing, while another one remains more or less unaffected by the change in the external

forcing. These different behaviors can only be sorted out by considering components individually.

In the following, the signal-to-noise ratio S will be calculated for individual components of $\mathbf{x}$. Because a coupled GCM will be used as the prediction model, components of $\mathbf{x}$ represent model variables (e.g., temperature, velocity) at model grid points. The result will be used to assess the question of which climate variable in what part of the world is potentially more predictable given an increase in CO_2 concentration under the perfect model approach. The answer obtained using the measure S is generally consistent with that obtained from the Kuiper statistic used by Anderson and Stern (1996), which focuses on the change in the distribution of the prediction ensemble (not shown).

It should be noted that predictability of the second kind can also be studied using a measure derived from "analysis of variance" (Zwiers 1996; Rowell 1998). This measure describes the percentage variance resulting from external forcing. The present study prefers S, which is directly related to the mean responses.

3. The prediction model and the ensemble integrations

A predictability study requires not only a predictability measure, but also a prediction model and the prediction and reference ensembles. This study uses the ECHAM5/Max Planck Institute Ocean Model (MPI-OM) atmosphere–ocean GCM developed at the Max-Planck Institute for Meteorology. The atmospheric component is the ECHAM5 model described by Roeckner et al. (2003). An earlier version of ECHAM is shown to represent the observed climate reasonably well (Roeckner et al. 1998). In the present study, the atmospheric component is run at the T31 spectral resolution with 19 levels. The main features of the oceanic component, MPI-OM, which includes a sea ice model, are provided by Marsland et al. (2003) and Jungclaus et al. (2005). The ocean model uses a curvilinear grid with the "North Pole" grid over Greenland and the "South Pole" grid over the Antarctic. The horizontal resolution varies from about 20 km near Greenland to about 350 km in the tropics. The grid allows a high resolution in the deep water formation regions of the Greenland, Labrador, and Weddell Seas. The two components are coupled without flux adjustments. A higher-resolution version of this coupled model is described in Jungclaus et al. (2006) and has been used to perform the scenario runs for the IPCC Fourth Assessment Report.

The reference ensemble is obtained from a multicentury integration with the ECAHM5/MPI-OM subjected

to the standard forcing with a constant CO_2 concentration of 280 ppm. Over the last 100 yr, the coupled system, in particular the atmosphere and the upper ocean are more or less in a stationary state. Figure 1 shows the yearly values of the maximum meridional overturning circulation at 30°N over the 100 yr. Assuming ergodicity, the states obtained from this 100 yr are used to form the reference ensemble. Because only yearly values are considered, the size of the reference ensemble n_r is 100. In Eq. (2), $\bar{x}_r$ is the mean over the 100 yr.

The prediction ensemble consists of predictions with the ECHAM5/MPI-OM under the same CO_2 forcing, but starting from different states in the 100-yr reference run. More precisely, the initial conditions are taken on 1 January of every second year in the 100-yr reference run. The years from which the initial conditions are drawn are marked by crosses in Fig. 1. The size of the resulting ensemble n_p is 50. Formulating the initial ensemble using states from a long control run is consistent with the fact that there are numerous states that are consistent with a given external forcing.

Starting from the collected initial conditions, each ensemble member has been integrated over 10 yr forced by a 3% increase in CO_2 concentration per year, starting from year 1. The 3% increase enhances the CO_2 level by a factor of 1.34 in year 10. Such a large forcing was chosen because of the initial apprehension that the coupled system may not respond noticeably within a short lead time of a few years. It will be shown later that some components respond astonishingly fast. For these components, the response in year 10 may not be approximated well by Eq. (1). This complication should be kept in mind when interpreting the response.

On the other hand, if Eq. (1) is appropriate, the responses discussed below would also apply to the case with, say, a 1% increase in CO_2 concentration per year. One needs only to reduce the 3% responses by factor $\ln(1.01)/\ln(1.03) \sim \frac{1}{3}$. The factor is obtained using Eq. (1), whereby taking $\partial\mathbf{x}/\partial\mathbf{F}|_0$ as the same for both the 1% and 3% forcing. Because the ensemble spread does not change much, the same scaling applies also to the values of S.

A CO_2 concentration of 280 ppm was chosen as baseline for the present study because a long integration with this CO_2 concentration was available at the time of experimental design. Strictly speaking, the sensitivity of a climate with 280 ppm is different from that of a climate with the present-day value of about 380 ppm. Shin et al. (2006) suggest that the atmospheric sensitivity may not change much between similar variations of atmospheric composition. A negligible change in sensitivity from 280 to 380 ppm has to be assumed when
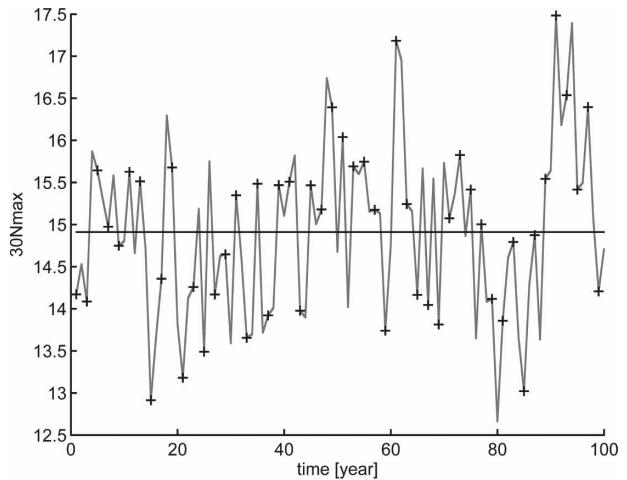

FIG. 1. Yearly time series of the maximum overturning streamfunction at 30°N (Sv) obtained from 100 yr of the control integration. The crosses indicate the years from which the initial conditions of the ensemble integrations were taken.

applying the result described below to the present-day situation.

It should be noted that this paper considers the CO_2 concentration as the only varying external forcing for the coupled system. Other greenhouse gases, such as methane, could enhance and the aerosol changes may offset the predictability found.

4. Potential predictability of the atmosphere

Significant potential predictability resulting from an increase in CO_2 concentration is found for air temperature. Figure 2 shows the signal-to-noise ratio for air temperature at 2 m in years 1, 4, 7, and 10. Given $n_r = 100$ and $n_p = 50$, the critical value at the 5% significance level equals 0.34. In Fig. 2 and all other maps of S, areas with $S > 0.34$ are shaded gray.

Already in the first year (Fig. 2a), potential predictability is identified over Eurasia. In year 4, significantly nonzero S is found in the subtropics. This subtropical signal, which extends more or less zonally, persists and intensifies with increasing lead time, whereby it is modified by some large signals over land. It stands out more clearly and remains zonally oriented over the Southern Ocean in year 10, because a zonal band of large S centered near 30°S is found. This band contrasts a zonal band of low values centered near 60°S, which are not significantly nonzero.

Figure 3 displays the ensemble mean differences in 2-m air temperature. As expected, the change is a warming over most part of the globe. In year 1, significantly nonzero S (gray areas in Fig. 2a) is associated with a warming over Eurasia and some cooling over the
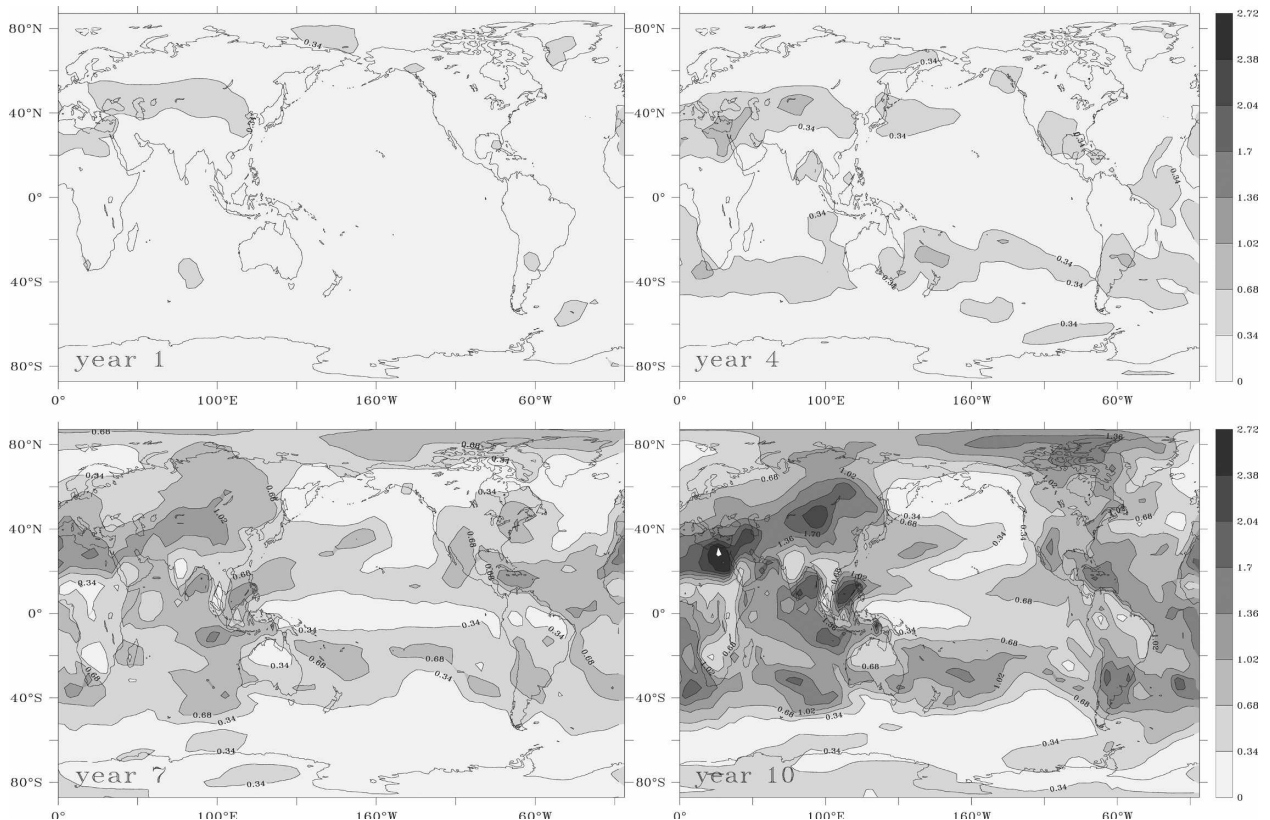
FIG. 2. Signal-to-noise ratio S for 2-m air temperature calculated according to Eq. (2). The gray shading indicates values larger than the critical value $S_* = 0.34$, obtained such that the probability for $S > S_*$ under the null hypothesis is smaller than 5%.

Arctic. With increasing lead time, the warming over Eurasia extends to most of the northern continents and covers the entire subtropical and tropical region from 40°N to 40°S. Over the Arctic, where there is a cooling in year 1, the air warms up at a speed faster than the warming over most of the other oceans. The ensemble mean differences in years 7 and 10 (lower panel in Fig. 3) reveal warming up to 1–1.5 K over land. Different from the changes in the Northern Hemisphere, changes in the Southern Hemisphere are more or less zonally symmetric. The associated warming in the southern subtropics and the slight cooling near 60°S suggest an increase in the meridional temperature gradient over the Southern Ocean.

Note that the increase in the meridional temperature gradient over the Southern Ocean, which is significant because of the significant increase north of 40°S, cannot be clearly seen when averaging the responses over two decades, as shown in IPCC AR4 Working Group 1 Final Report (their Fig. 10.8; Meehl et al. 2007).

By and large, areas with large signal-to-noise ratio coincide with areas with large ensemble mean difference shown in Fig. 3. Notable exceptions are found over the northern mid- and high-latitude land, where a large ensemble spread over land is found. As a result, the largest value of S of about 2.5 occurs over North Africa, while the largest warming of about 1.5°C is found over the Tibetan Plateau and in some northern spots of Eurasia and North America.

For many variables, area-averaging leads to an increase in signal-to-noise ratio. This is particularly true for temperature. Figure 4 shows the result for zonally averaged 2-m air temperature, along with ±one standard deviation ($\pm\hat{\sigma}_p$) of the zonal mean 2-m temperature in year 10 (shading). The shading shows how ensemble spread in year 10 changes with latitudes. Consistent with the assumption that the spread of the prediction ensemble equals the spread of the reference ensemble, $\hat{\sigma}_p$ strongly resembles the spread in the reference run ($\hat{\sigma}_r$) and changes little with lead time (not shown).

In the southern subtropics and tropics, the ensemble mean difference in Fig. 4a has essentially the same magnitude as that in Fig. 3. Despite of that, the signal-to-noise ratio for zonally averaged temperature is about 3 times larger than for gridpoint temperature, suggesting
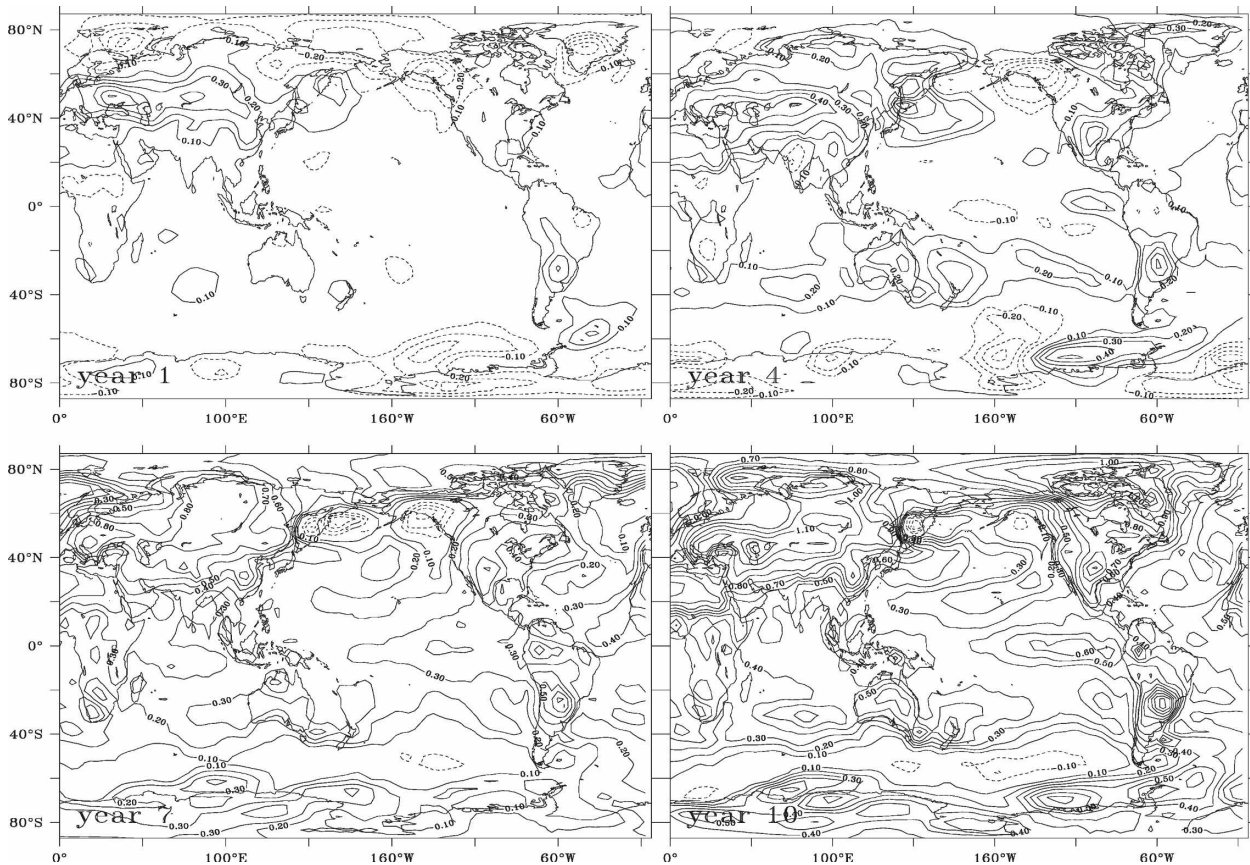
FIG. 3. Ensemble mean difference $\bar{x}_p - \bar{x}_r$ for 2-m air temperature in year (top left) 1, (top right) 4, (bottom left) 7, and (bottom right) 10 (°C). The isoline interval is 0.1°C. Solid (dashed) lines indicate positive (negative) values. Zero line is not plotted.

that zonal averaging significantly reduces the ensemble spread. In fact, the subtropics near 30°S are one of the two places where the zonal mean air temperature has the smallest spread. The result suggests that the zonally averaged temperature is potentially more predictable than gridpoint temperature. The most significant increase in 2-m temperature at about 30°S, together with a near-zero change at about 55°S, further confirm the increase in the meridional temperature gradient over the Southern Ocean.

The meridional profiles given in Fig. 4 do not vary substantially with height (not shown). In particular, an increase in meridional temperature gradient over the Southern Ocean can be identified throughout the troposphere. This is because, on the one hand, the ensemble mean change in the zonally averaged temperature increases with height in the tropics and reaches the largest value of about 1°C near 200 hPa in the tropics, and on the other hand, the minimum change centered near 60°S extends to about 300–400 hPa.

The increase in temperature gradient is accompanied by changes in the zonal mean zonal wind. Because

these changes are essentially barotropic, Fig. 5 shows only the vertical average of zonal mean zonal wind, along with ±one standard deviation ($\pm\hat{\sigma}_p$) of the zonal mean zonal wind in year 10 (shading). The largest positive changes describe an intensification of the mean westerly jet over 50°–60°S (Fig. 5a). The associated signal-to-noise ratio S is significantly nonzero and reaches maximum values of about 0.7–0.8 after year 4 (Fig. 5b). North of 40°S, some negative changes are found. They could, together with the positive changes centered near 50°–60°S, suggest a southward shift of the zonal mean zonal wind. However, they are hardly significant at the 5% level.

Different from air temperature, the response in the zonal mean zonal wind does not gradually increase with increasing lead time. The response in year 10 (black) is not the largest, and the response in year 4 (dark blue) is comparable to those in the last 3 yr. The amplitude of S (Fig. 5a) evolves similarly with lead time.

The changes in the zonal mean zonal wind are related to changes in the intensity and location of the Ferrel cells. This is shown by the ensemble mean difference in
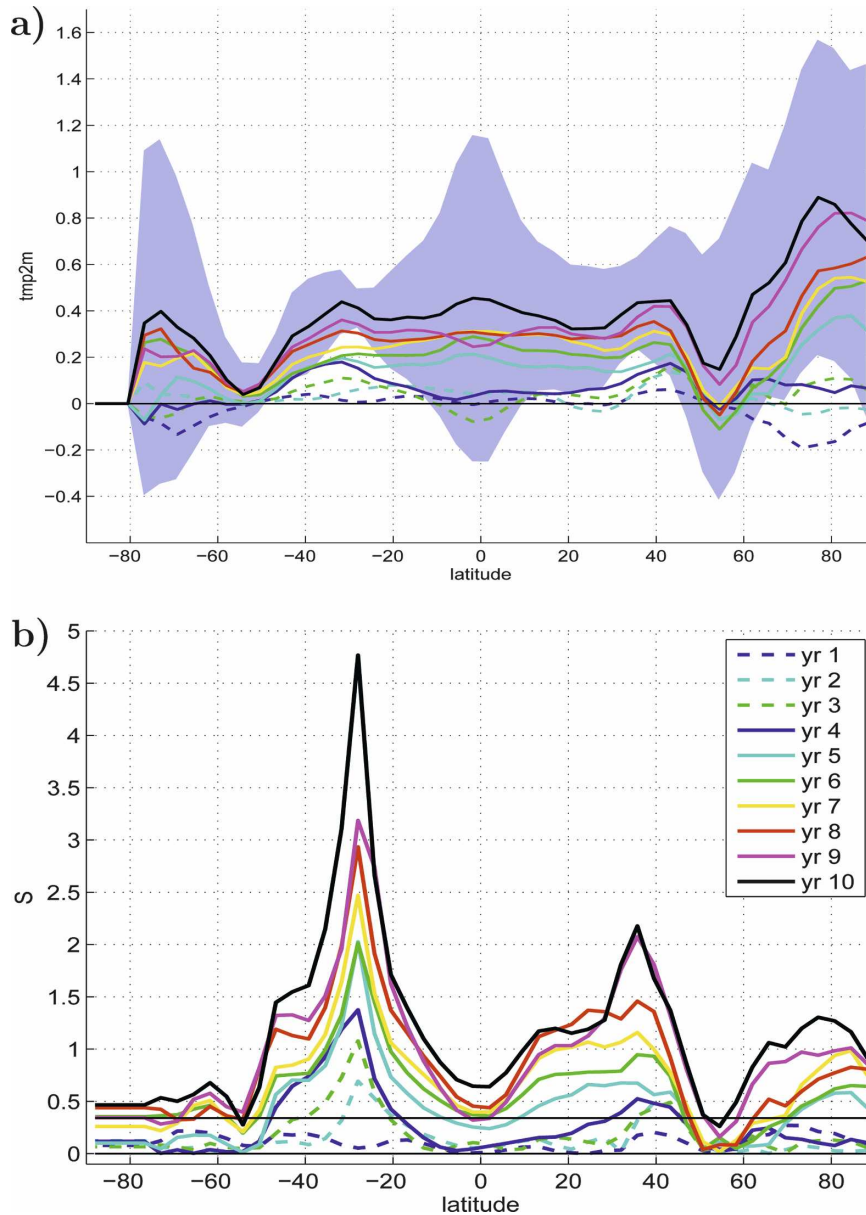
FIG. 4. (a) Ensemble mean difference in zonally averaged 2-m air temperature (°C) and (b) the respective signal-to-noise ratio. The horizontal line in (b) indicates $S_* = 0.34$, the same critical value explained in Fig. 2. In both (a) and (b), the results for each year are shown with the same color codes as indicated in the box in (b). The shaded area in (a) is the ± 1 std dev ($\pm \overline{\sigma}_p$) in year 10.

the vertically and zonally averaged vertical velocity ω in Fig. 6a. Systematic changes are found over the Southern Ocean, characterized by descending motion (positive ω) centered at 40°S and ascending motion (negative ω) between 50° and 80°S. In the reference ensemble, the descending branch of the Hadley cell and the Ferrel cell extends from 15° to 40°S and the ascending branch of the Ferrel cell and the polar cell extends from 40° to 65°S. Comparing this structure of the ref-

erence ensemble with the ensemble difference in Fig. 6a suggests an intensification and somewhat southward shift of the Ferrel cell. The signal-to-noise ratio (Fig. 6b) suggests that the intensification of the ascending branch of the Ferrel cell is significant in the last 5 yr.

5. Potential predictability of surface fluxes

This section considers the potential predictability of the fluxes of heat, freshwater, and momentum into the
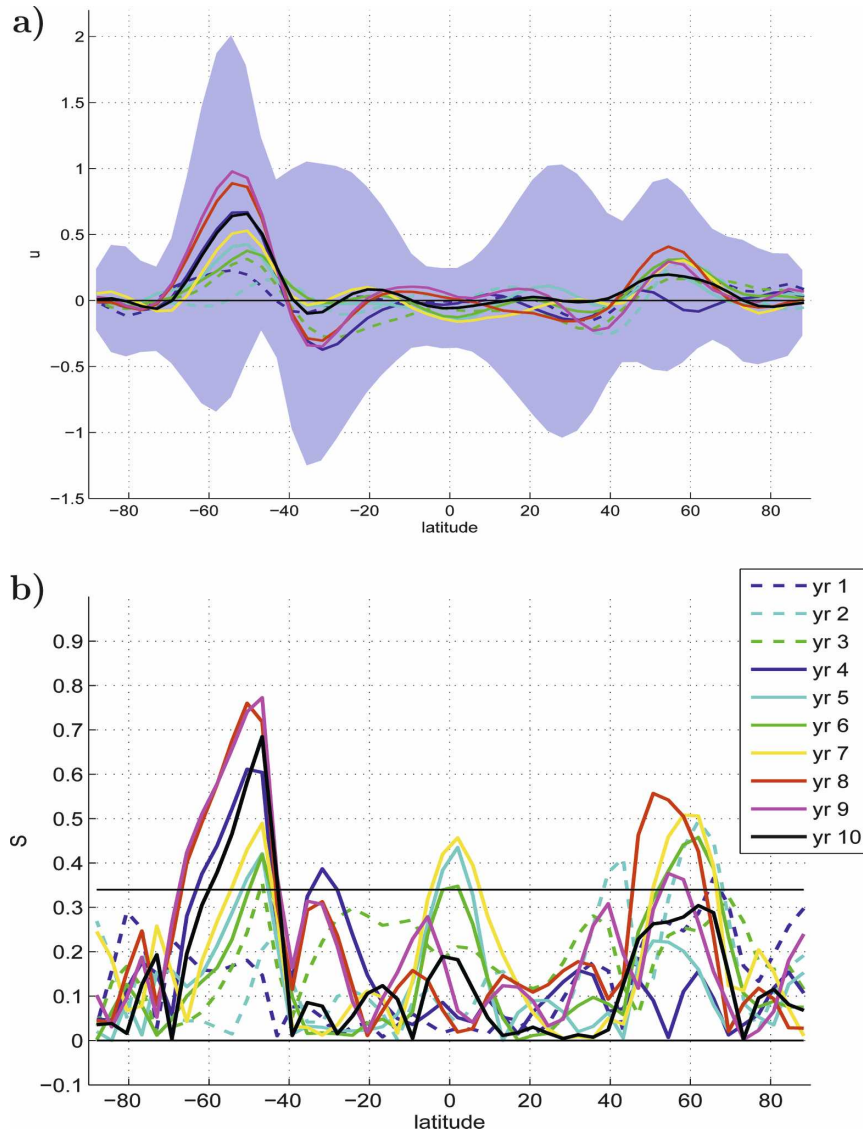
a)

b)

FIG. 5. Same as Fig. 4, but for vertically and zonally averaged zonal wind. The unit in (a) is
m s^{-1}.

oceans resulting from the increase in CO_2 concentration. For all surface fluxes, there is hardly any notable signal-to-noise ratio in the first 2–3 yr. As lead time further increases, a gradual increase in potential predictability is found. Figure 7a shows the situation for the total downward heat flux in year 10. Predictability is found predominantly over the Southern Ocean between 40° and 60°S and over the Arctic. Other areas with potential predictability are the Indonesia region, partially the central equatorial Pacific, and some spots in the North Pacific and the North Atlantic between 40° and 60°N. No significant change in the net downward heat flux is found in the subtropical Pacific and the subtropical Atlantic. The maps of ensemble mean

differences show that the signal is characterized by a gradual increase in downward (positive) heat flux with increasing lead time (not shown). The largest difference reaches about 5–15 W m^{-2} in year 10 (Fig. 7b) over the areas with significantly nonzero signal-to-noise ratio.

Comparing Fig. 7 with the result of the last section suggests that an increase in downward heat flux does not occur in places with the strongest tropospheric warming: The large and significant increase in the downward heat flux occurs over the Southern Ocean and partly in the northern North Atlantic and North Pacific, where the warming signal is the smallest (lower right plot in Fig. 3), while smaller and insignificant
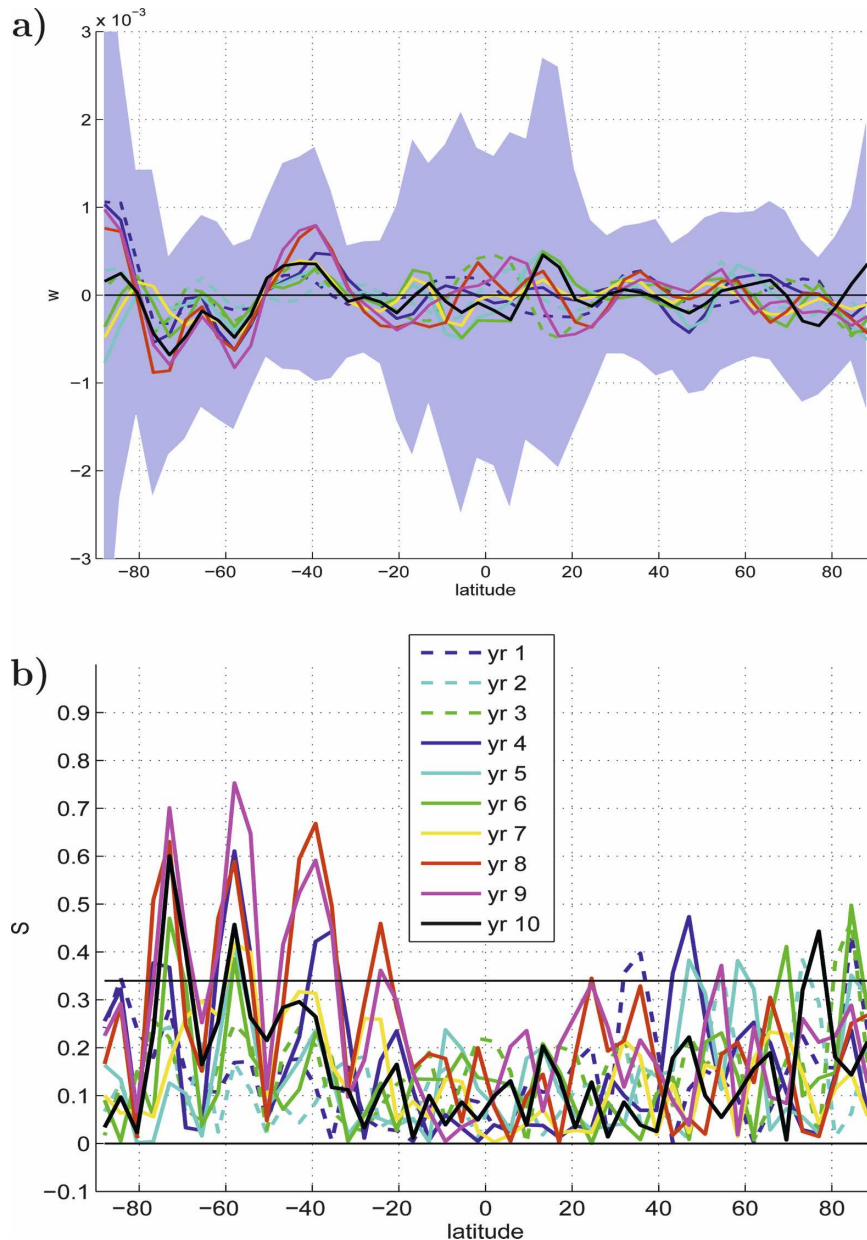
FIG. 6. Same as Fig. 4, but for vertically and zonally averaged vertical velocity. Positive values indicate downward movements. The unit in (a) is Pa s^{-1}.

changes in the downward heat flux are found in the subtropics, where the largest significant warming signal is located (Fig. 4). Thus, an increase in air temperature does not lead to a local increase in the downward heat flux into the ocean.

The just mentioned feature becomes more apparent when considering heat flux zonally averaged over the oceans (not shown). The largest increase in downward heat flux occurs at around 55°N and 55°S, where the increase in 2-m air temperature is the smallest (Fig. 4).

The smallest increase on the other hand occurs in the subtropics around 30° in both hemispheres, where secondary maxima in 2-m air temperature changes are found. The zonal average notably enhances the signal-to-noise ratio, and results in $S = 1.6$ near 55°S and $S = 1$ near 55°N in year 10.

Integrated globally, one finds a gradual increase in the net downward heat flux (green line in Fig. 8). By year 10, this heat flux reaches 440 TW (10^{12} watts). The increase is by and large linear. To have some idea about
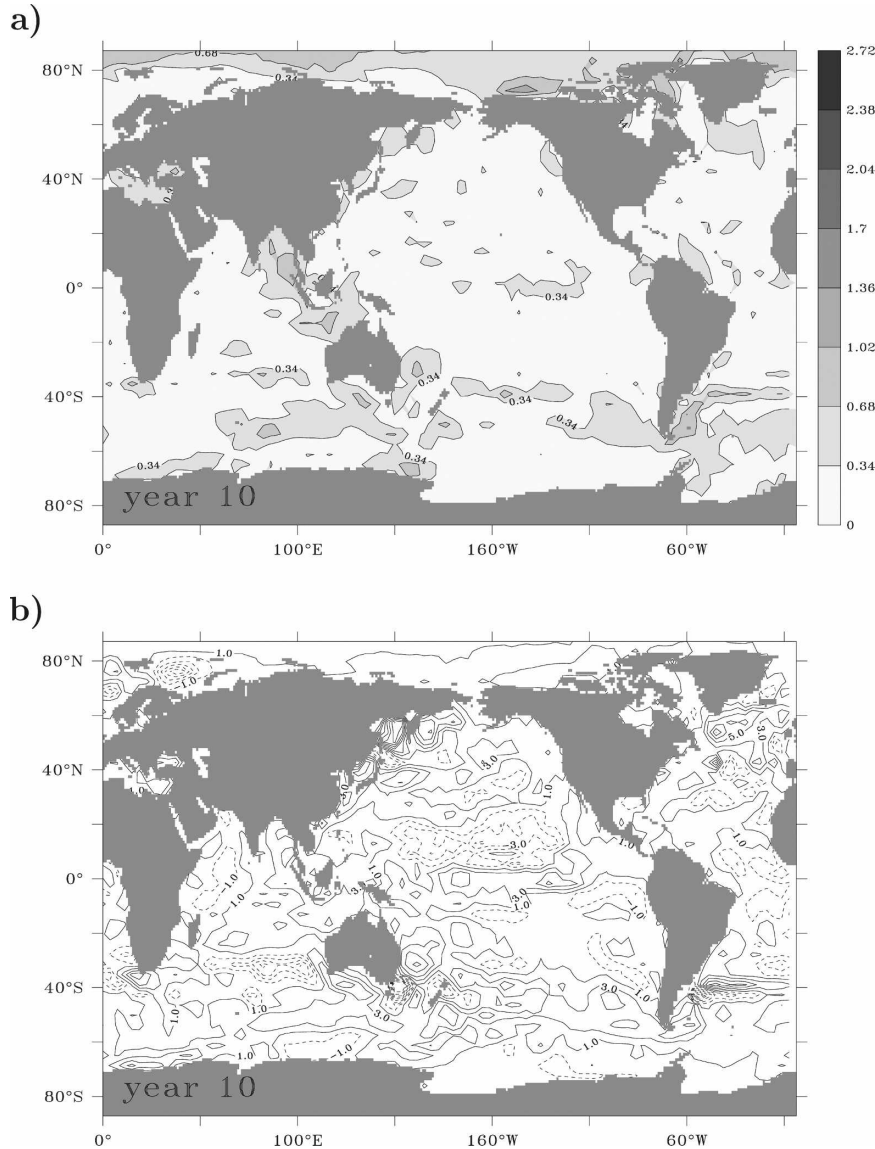
a)

b)

FIG. 7. (a) Signal-to-noise ratio S for the total heat flux (i.e., the sum of the sensible, latent, and radiative fluxes) in year 10 and (b) the ensemble mean difference $\bar{x}_p - \bar{x}_r$ in year 10. The isoline interval in (b) is 2 W m^{-2}. Solid (dashed) lines indicate positive (negative) values. Zero line is not plotted. Positive (negative) values indicate enhanced downward (upward) heat flux. The signal-to-noise ratio is plotted in the same way as in Fig. 2.

how much of this amount of heat flux is inputted into different oceans, various area integrals are calculated. Figure 8 shows that about one-third of the total downward heat flux enters the Southern Ocean between 38° and 65°S (red) and only a small portion enters the northern North Atlantic (blue).

If the net heat flux of 440 TW in year 10 results from a linear increase with time, and if this heat flux is distributed uniformly over the ocean area, one would have an increase in heat flux of about 1.2 W m^{-2} in 10 yr, or $c = 0.12$ W m^{-2} yr^{-1}. Here, c is obtained by fitting a

linear trend into the evolution of the globally integrated heat flux. In the case that the ocean consists only of a mixed layer of depth h, the change in SST after 10 yr can be calculated using

$$\frac{d(\text{SST})}{dt} = \frac{Q(t)}{h c_p \rho}, \tag{5}$$

where t is time, c_p is the specific heat, and ρ the density of seawater. Using $Q(t) = c \times t$, with $c = 0.12$ W (m^2 yr)$^{-1}$, $c_p = 4000$ J (kg C)$^{-1}$, and $h = 88.6$ m, which
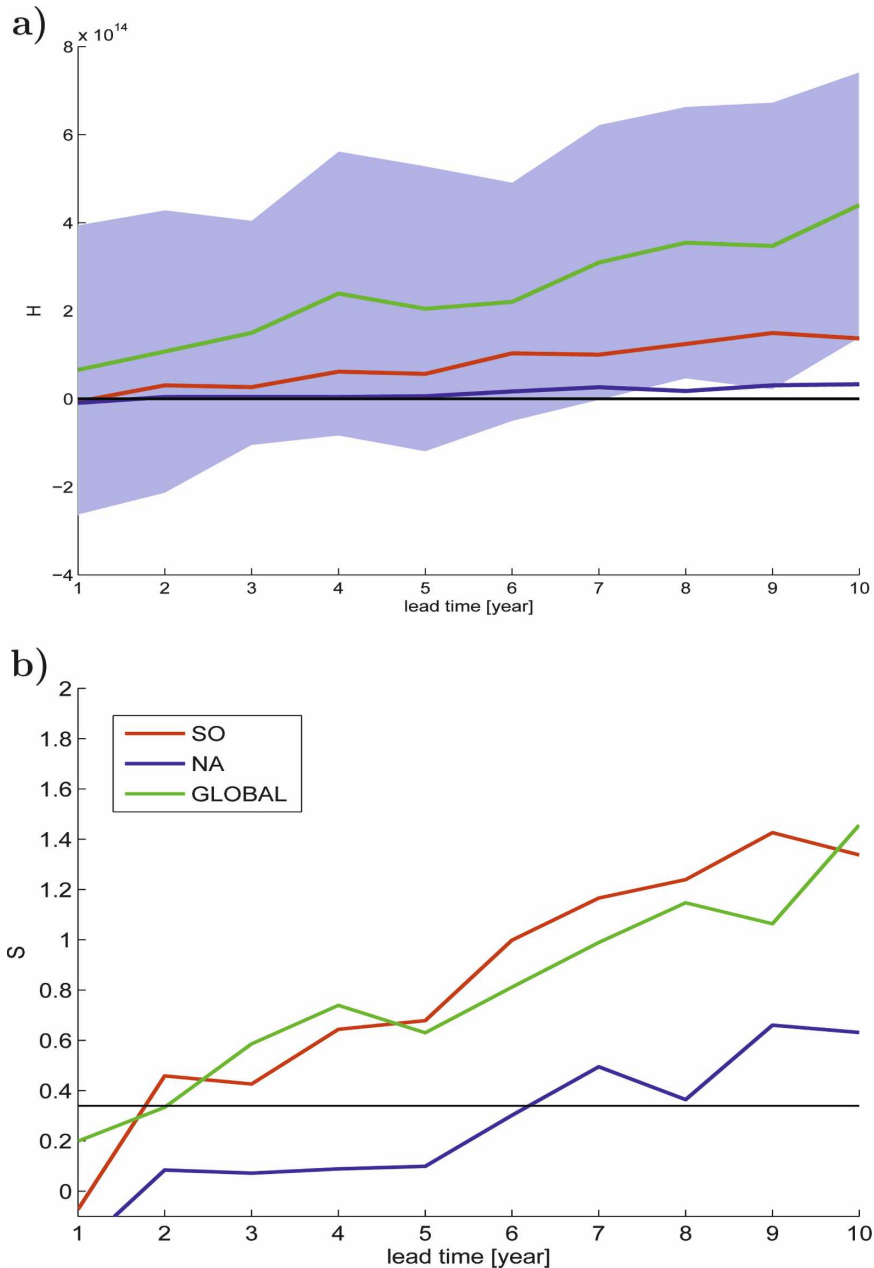
FIG. 8. (a) Ensemble mean difference (in W) and (b) the signal-to-noise ratio for the total heat flux integrated over the global ocean area (green), the Southern Ocean (red), and the northern North Atlantic (blue) as function of lead time t. The shading indicates the spread of the prediction ensemble for the globally integrated total heat flux. The Southern Ocean area used for the integration extends from 38° to 65°S and that for the northern North Atlantic from 38° to 72°N.

equals the mean mixed layer depth in the reference run, the solution of Eq. (5) gives a globally averaged SST increase of about 0.53°C in year 10. This number is about twice as large as 0.26°C, the global mean SST change obtained from ensemble mean difference in year 10 shown in section 6.

Also shown in Fig. 8 is the net heat flux into the northern North Atlantic from 38° to 72°N (blue), an area where the increase in the downward heat flux could affect the static stability, and consequently the deep water formation. There is a gradual increase of downward heat flux into the northern North Atlantic.

a)

b)
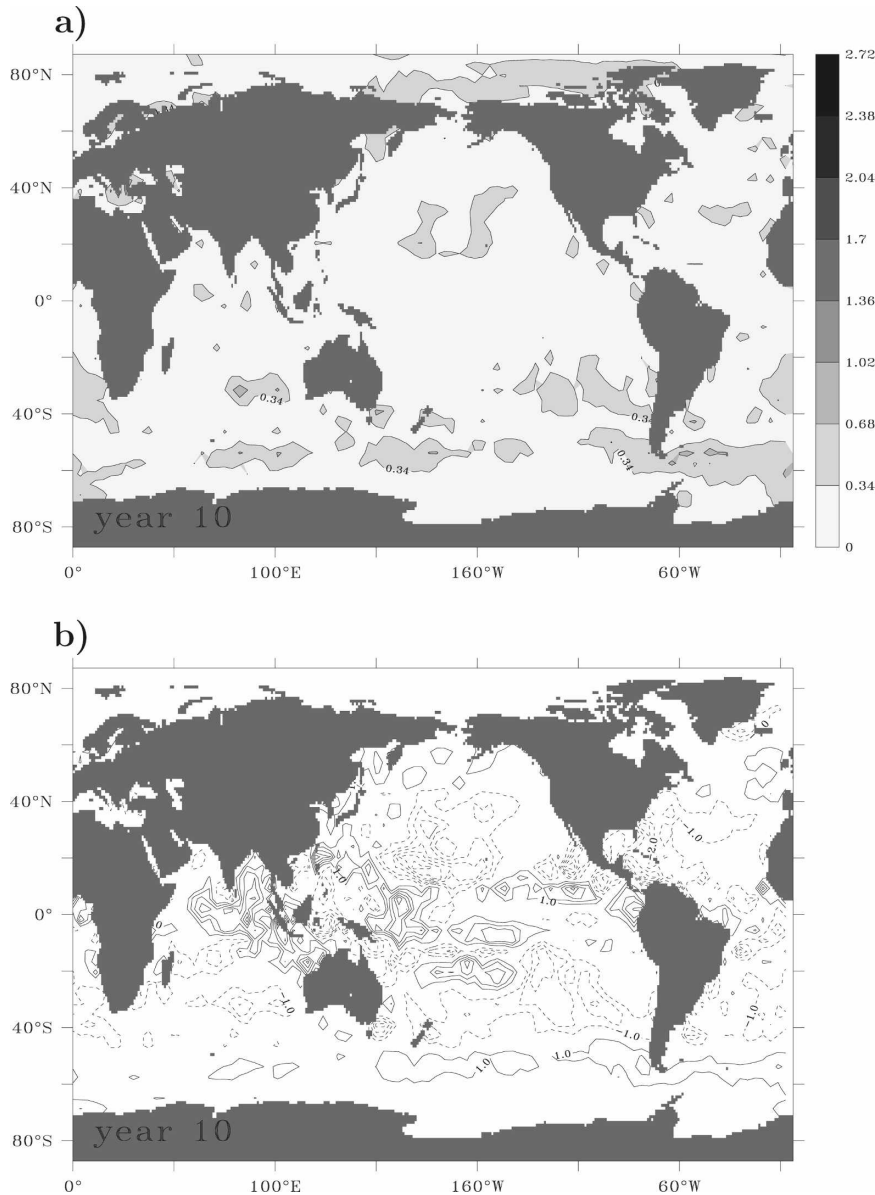
Fig. 9. Same as Fig. 7, but for the net freshwater flux (precipitation minus evaporation) in 10^{-6} kg s^{-1}. The isoline interval is 1×10^{-6} kg s^{-1}. Solid (dashed) lines indicate positive (negative) values. Zero line is not plotted.

The signal-to-noise ratio is significantly nonzero in year 6 and onward.

The CO$_2$ increase also leads to potential predictability for the net freshwater flux (precipitation minus evaporation). Figure 9a shows that significantly nonzero signal-to-noise ratio S is found in two separate bands over the Southern Ocean in year 10—one centered near 35°S and the other near 60°S. Nonzero values of S are also found in the central North Pacific, in some spots in the northern North Atlantic and over the Arctic. The nonzero values of S are related to a net downward freshwater flux (precipitation excess evaporation) over a band centered near 60°S in the Southern Ocean, the Arctic, and the northern North Pacific and northern North Atlantic, and a net upward freshwater flux (evaporation excess precipitation) over most of the subtropical oceans (Fig. 9b). The largest changes occur in the tropics. However, because of the large variability there, these changes are not significant.

The general tendency to have a latitudinal dipole, characterized by an increase in downward freshwater flux at mid- and high latitudes and an increase in up-

ward flux in the subtropics, is more clearly demonstrated using zonal averages. This is the case in particular in the Southern Hemisphere, where the signal-to-noise ratio of zonally averaged flux is about 4 times larger than the values shown in Fig. 9 and reaches maximum values of about 1 (not shown). The significance of the dipole structure is consistent with a warming in the southern subtropics (Fig. 4), which allows the atmosphere to contain more water vapor in favor of evaporation (i.e., negative changes in freshwater flux), and the strengthening of the westerlies, which could lead to strengthening of the storm track and the related precipitation, leading to positive changes in freshwater flux. In the Northern Hemisphere, zonal averaging also results in an increase in the signal-to-noise ratio, which confirms the dipole structure with the ocean losing freshwater in the subtropics and gaining at midlatitudes. However, the Northern Hemisphere signal is much weaker than that in the Southern Hemisphere.

The global integral of the net freshwater flux (green in Fig. 10) shows negative values (i.e., enhanced upward freshwater flux), in particular for lead times larger than 5 yr. The value in year 10 corresponds to 0.03 Sv ($1 \text{ Sv} \equiv 10^6 \text{ m}^3 \text{ s}^{-1}$). The enhanced upward flux is associated with the increased evaporation in the subtropics. This is suggested by the net freshwater flux into the subtropical band extending from 13° to 42° in both hemispheres (red). The situation in the North Atlantic is characterized by an increase in upward flux in the subtropics (black) and a tiny increase in the downward flux in the subpolar region (blue). The latter is not significant at 5% significance level.

The potential predictability of zonal wind stress concentrates mainly over the Southern Ocean (Fig. 11). Consistent with changes in the westerly winds in the Southern Hemisphere, the zonal wind stress increases between 50° and 60°S and decreases around 40°S. Different from the vertically averaged zonal mean zonal wind, not only the increase but also the decrease is at least partially significant in year 10. Applying zonal averaging enhances the signal-to-noise ratio and results in two maxima with significantly nonzero S in year 4 and the last 3 yr, one centered near 35°S and the other near 55°S. The result suggests intensification and a southward shift of the zonal wind stress. The signal-to-noise ratio does not increase linearly with lead time. Instead, it evolves in a way similar to the vertically and zonally averaged zonal wind, for example, having a notably large value in year 4, but not the largest value in year 10.

The strengthening and poleward shift of zonal wind stress are found in twentieth- and twenty-first-century simulations performed with different climate models

(Fyfe and Saenko 2006). This suggests that the wind stress signal is not a feature of the particular model used.

The fact that the signal-to-noise ratio is notably larger for zonally averaged fluxes than for gridpoint fluxes is an indication that the response of surface fluxes to an increase in CO_2 concentration is primarily zonally orientated.

6. Potential predictability of the ocean

The increase of heat flux into the northern North Atlantic becomes significant from year 6 onward. This increase could lead to a reduction of the Atlantic meridional overturning circulation (MOC). The consideration of a zonally averaged streamfunction suggests that this is not the case (not shown).

What does change significantly is the wind-driven Ekman circulation in the upper ocean. Figure 12 shows the ensemble mean changes in zonally averaged meridional velocity in the first five model layers in year 10. The largest change in the zonally averaged meridional velocity is an increase in northward velocity from about 40° to 60°S and a decrease north of 40°S. These velocity changes are consistent with the changes in the zonal wind stress τ_x (Fig. 11) that favor a strengthening in the northward Ekman transport from 40° to 60°S and a strengthening of the southward Ekman transport north of about 40°S. The signal-to-noise ratio further confirms the role of wind forcing by showing that the velocity changes in the surface layer is only significant in the years when the change in the atmospheric circulation is the largest, that is, in year 4 and in the last 3 yr (not shown).

The changes in the meridional Ekman transport can be responsible for the changes in SST. Figure 13 shows the ensemble mean changes in the zonally averaged SST (top) and grid point SST in year 10 (bottom). The global average of the change is 0.26°C in year 10. The meridional profiles within 60°S and 60°N resemble, to a large extent, those of the 2-m air temperature, with the only difference being the much larger increase at the northern high latitudes for air temperature than for SST. Thus, the increase in meridional gradient in air temperature discussed in section 4 is directly coupled to the increase in meridional gradient in SST. Similar to the air temperature, the meridional profile of the changes in SST does not follow that of the downward heat flux (Fig. 7). Little warming occurs at the 50°–55°S latitudes where large increases in the downward heat flux are found, whereas large warming takes place at about 30°S, where the change in the downward heat flux is small. This meridional profile, which would not

a)

b)
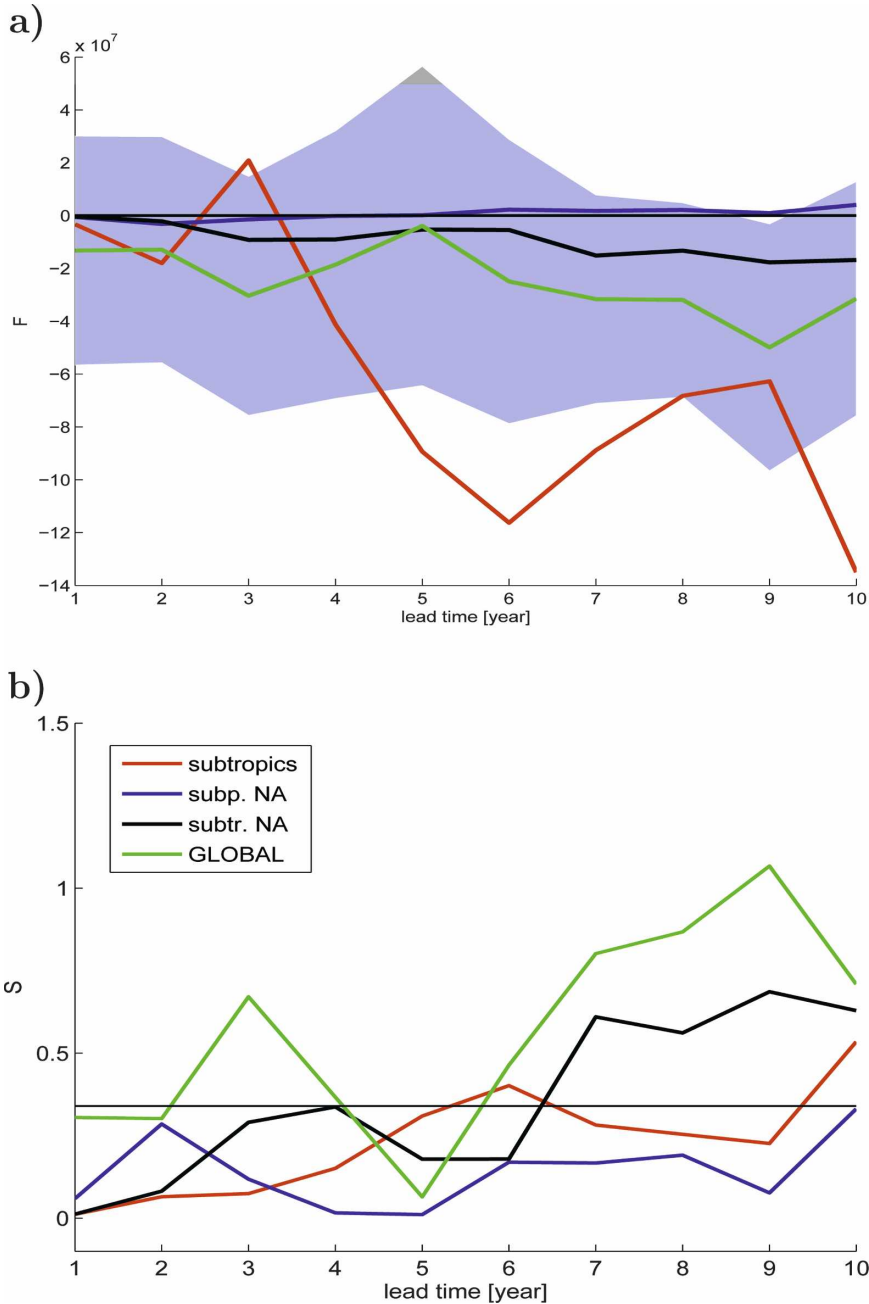
FIG. 10. (a) Ensemble mean difference (kg s^{-1}) and (b) signal-to-noise ratios for freshwater flux integrated over the global ocean area (green), the subtropical oceans (red), and the northern (blue) and subpolar (black) North Atlantic as function of lead time t. The shading indicates the spread of the prediction ensemble for the globally integrated freshwater flux.

be obtained if SST changes were directly forced by the change in the downward heat flux, is likely the result of the meridional Ekman transport. The southern latitudes with little SST changes represent the region where the mean (not shown) and the enhanced northward Ekman transport (Fig. 12) are found. Given the strong mean surface temperature gradient from the

subtropics to about 60°S in the reference run (not shown), the mean and the enhanced northward transport can significantly reduce the effect of the increased downward heat flux by persistently importing cold water from high latitudes into this region. On the other hand, the enhanced southward Ekman transport north of 40°S can increase the SST, thereby persistently im-
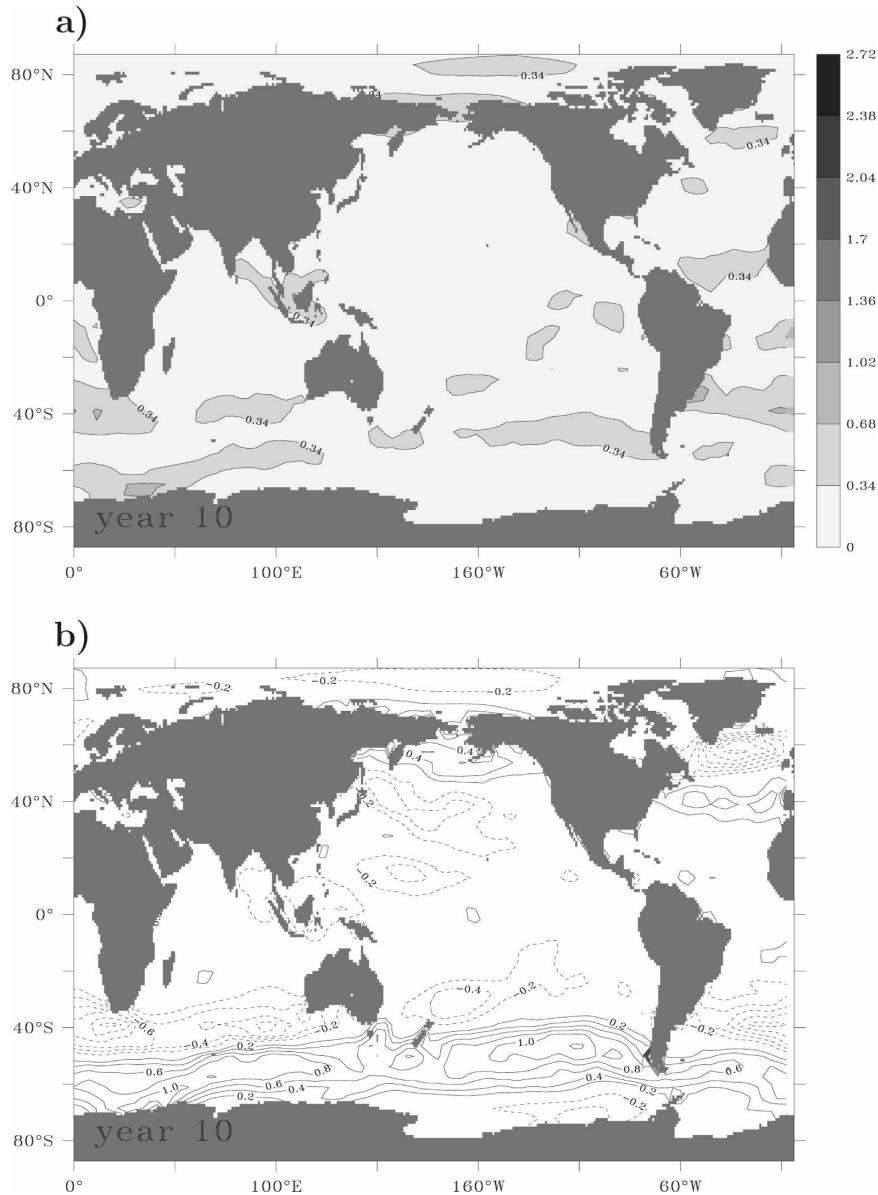
FIG. 11. Same as Fig. 7, but for zonal wind stress (10^{-2} Pa). The isoline interval is 0.2×10^{-2} Pa. Solid (dashed) lines indicate positive (negative) values. Zero line is not plotted.

porting warmer water from the subtropical region, despite a weaker increase in the net downward heat flux.

Note that both sea ice cover and sea ice thickness did not notably change over the 10-yr prediction time period (not shown). This is consistent with the suggestion that changes over the Southern Ocean are related to interactions between atmosphere and ocean, without involving changes in sea ice.

The situation is somewhat different in the North Pacific and North Atlantic. There an enhancement of poleward velocity is found near 60°–70°N (Fig. 12). This change works to increase the SST near 60°–70°N (Fig.

13), making the increase in temperature gradient much less pronounced than in the Southern Ocean.

The above discussion suggests only that changes in the wind stress over the Southern Ocean can significantly affect the changes in the meridional distribution of SST. The question remained to be answered is whether and how the warming signal at the surface is propagated downward to the deep ocean.

The signal-to-noise ratio of zonally averaged ocean temperature (Fig. 14) suggests a fast downward propagation. Significantly nonzero values of S are found down to about 1000–3000 m at about 40°S in year 5 and

FIG. 12. Ensemble mean difference in zonally averaged meridional velocity (cm s^{-1}) in the first five model layers in year 10. The isoline interval is 0.04 cm s^{-1}. Solid (dashed) lines indicate positive (negative) values. Zero line is not plotted.

onward. Similar deep-penetrating structure of nonzero values of S also emerges near 40°N. The warming signal seems to propagate through two "corridors" located near 40°S and 40°N that extend from the surface to about 3000–3500 m. Outside the corridors, no significant increase in temperature is found in the deep ocean. The downward propagation does not seem to be related to the changes in the atmospheric circulation, because the downward propagation signal gradually increases with lead time, rather than being particularly large in years (e.g., in year 4) when large changes in wind stress are found. The magnitude of the warming reaches 0.3°C near the surface and 0.05°–0.1°C in the deeper ocean (Fig. 15).

It is noted that the deep ocean in the reference run reveals a drift. For the temperature, the amplitude of the drift can be on the order of 0.02°C decade^{-1}. When starting the prediction experiments from the states in the reference run, the deep ocean continues to drift, independent of the changes in the CO$_2$ forcing. To obtain the signal that originates from the changing CO$_2$ forcing only, a mean linear drift is estimated from the 100 yr of the reference run and subtracted from the prediction experiments before performing the calculations that result in Figs. 14 and 15.

There are three ways for the warming signal to be transported down into the deep ocean, namely, via vertical advection, convective mixing, and vertical diffusion. The mean vertical velocity is downward near 40°S and 40°N. However, it is too small for vertical advection to be important. Given a typical vertical velocity on the order of 10^{-6} m s^{-1}, it will take about 63 yr for a signal

at the surface to be advected over a distance of 2000 m into the ocean interior. This certainly cannot explain the much faster downward propagation suggested by Fig. 14.

The convective mixing is parameterized in MPI-OM by a strong vertical diffusion, which is switched on in case of static instability. The respective diffusion coefficient is 10^{-1} m^2 s^{-1}, which generally dominates the other processes that also contribute to the vertical diffusion (to be discussed below). Thus, if the changing CO$_2$ forcing induces a change in convective activity, one would obtain large changes in the total vertical diffusion. As will be discussed below, the total vertical diffusion near 40°S and 40°N decreases with increasing lead time.

In principle, vertical diffusion can be responsible for downward propagation of a surface signal. In MPI-OM, temperature diffusion consists of two components—an isoneutral–dianeutral component and a vertical component. The vertical diffusion coefficient is, in static stable situation, a function of a Richardson number–dependent mixing, a wind-induced mixing, and a background diffusivity. The background diffusion is set to 10^{-5} m^2 s^{-1}. The wind-induced mixing, which can in principle be of the order of 10^{-1} m^2 s^{-1} and be affected by wind changes discussed in section 4, is confined to the first 40 m. Thus, below 40 m and outside convective regions, a change in the vertical diffusion coefficient is determined by the change in the Richardson number–dependent mixing only.

Even though vertical diffusion can in principle bring the warming signal downward, it might not be of pri-
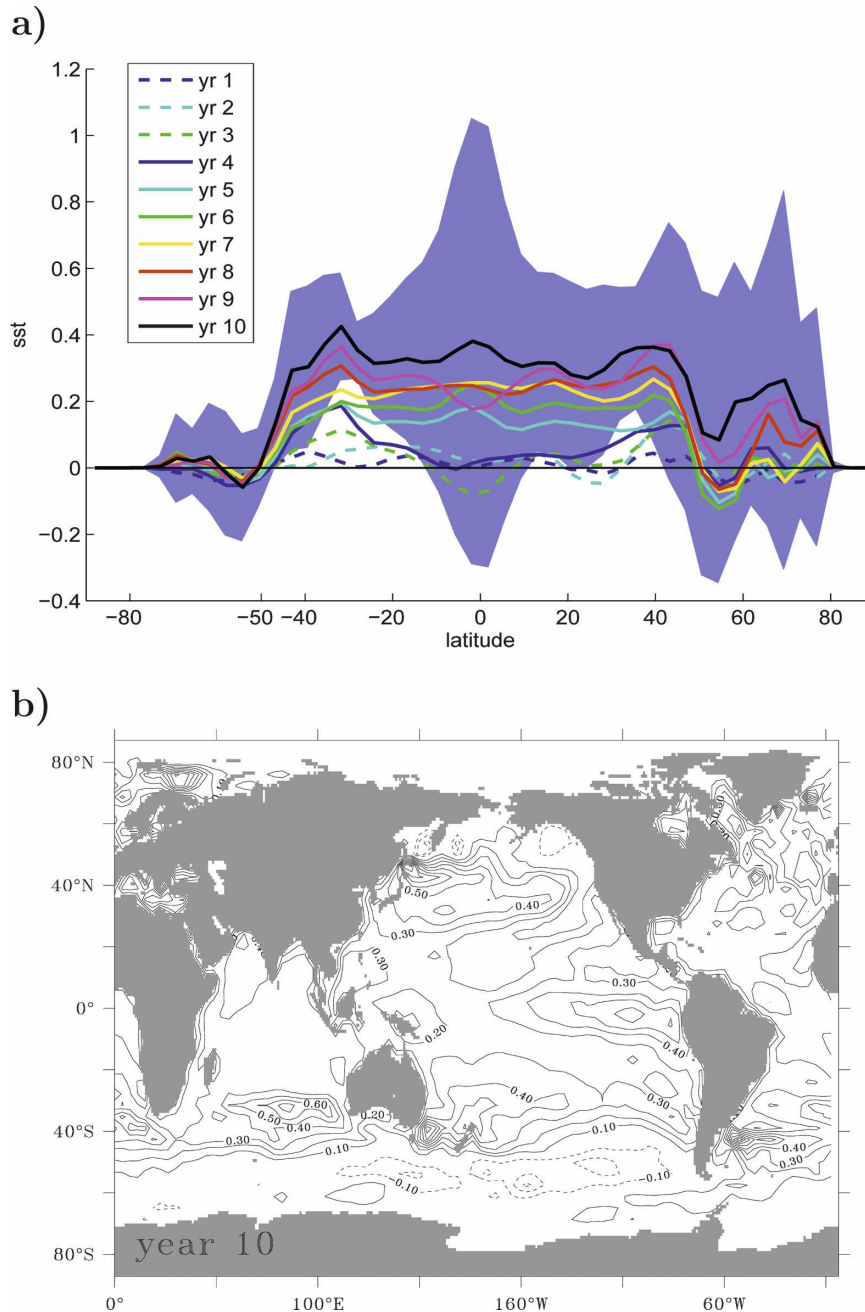
FIG. 13. (a) Ensemble mean difference in zonally averaged SST (C°) and (b) ensemble mean difference in SST in year 10. In (b), the isoline interval is 0.1 C°. Solid (dashed) lines indicate positive (negative) values. Zero line is not plotted.

mary importance. The ensemble mean changes in the total vertical diffusion coefficient reveal notable decreases at the midlatitudes from the first a few hundred to 1000 m (not shown). This reduction, likely caused by a general increase in the stability of the ocean resulting from the surface warming, does not fit to the gradual increase in downward propagation with increasing lead time.

The isoneutral–dianeutral diffusion makes use of a rotation of the diffusion tensor from horizontal–vertical directions to neutral and dianeutral directions (Redi 1982) and is numerically implemented following Griffies et al. (1998). The strength of the isoneutral diffusion depends linearly on the grid size and equals 1000 $m^2 s^{-1}$ for $\Delta x = 400$ km, which is about the largest grid size. Thus, isoneutral mixing is much stronger than the
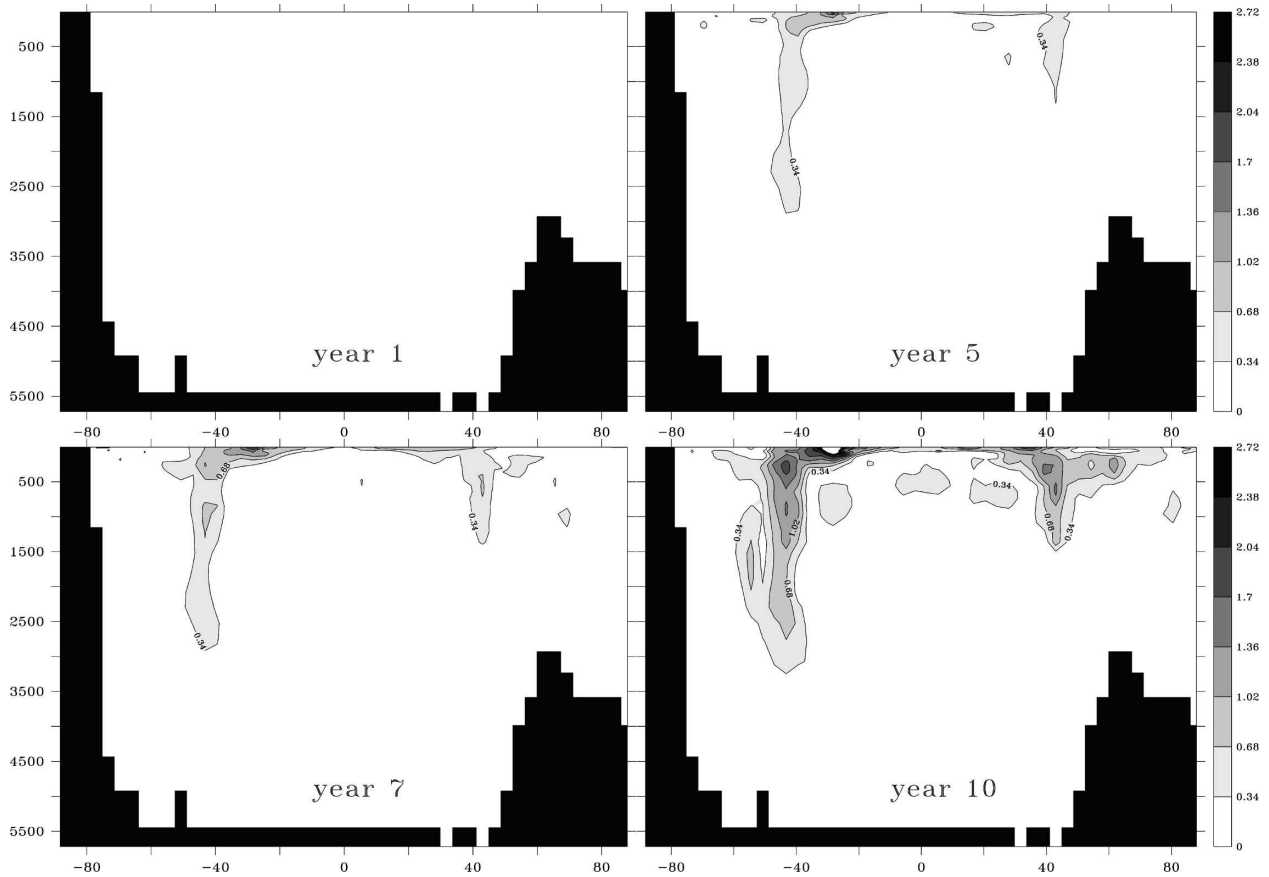
FIG. 14. Signal-to-noise ratio for zonally averaged ocean temperature as function of latitude and depth in year (top left) 1, (top right) 5, (bottom left) 7, and (bottom right) 10.

vertical mixing. In regions where the surface of neutral density is tilted toward the vertical direction, isoneutral mixing will effectively diffuse the surface warming signal down to the deeper ocean.

The isoneutral surfaces are related to the surfaces of potential density. The mean zonally averaged potential density in the reference run (Fig. 16) identifies two regions where the isopycnals are strongly tilted toward the vertical direction. One is located at about 40°S and the other at 40°N. The two regions coincide with the "corridors" through which the surface warming is propagated downward (Fig. 14), suggesting the dominant role of isoneutral mixing for the downward propagation of surface signal.

It is noted the above consideration is based on the analysis of yearly data. The situation could be different when considering processes on time scales shorter than 1 yr. For these processes, the mean vertical mixing obtained from the reference run under the control condition could play an important role.

To this end, it is worthwhile to revisit the rough-and-dirty estimate of the effect of the increased net down-

ward heat flux in section 5. Using Eq. (5) again, one finds that if the mixed layer of about 88.6-m thickness receives only half of the increased heat flux (i.e., 200 TW instead of 400 TW in 10 yr), then the globally averaged SST would be about the same magnitude as obtained from the coupled model. This suggests that, in order to arrive at the globally averaged SST value produced by the coupled model, half of the increased net heat flux must be efficiently removed from the mixed layer and transported down into the deep ocean within short time. The representation of mixing processes could affect the efficiency of the downward propagation of heat.

7. Discussion and conclusions

a. Potential predictability resulting from external forcing

One important difference between predictability of the first and second kind is that predictability of the first kind generally decreases with lead time because of uncertainty in the initial condition, while predictability
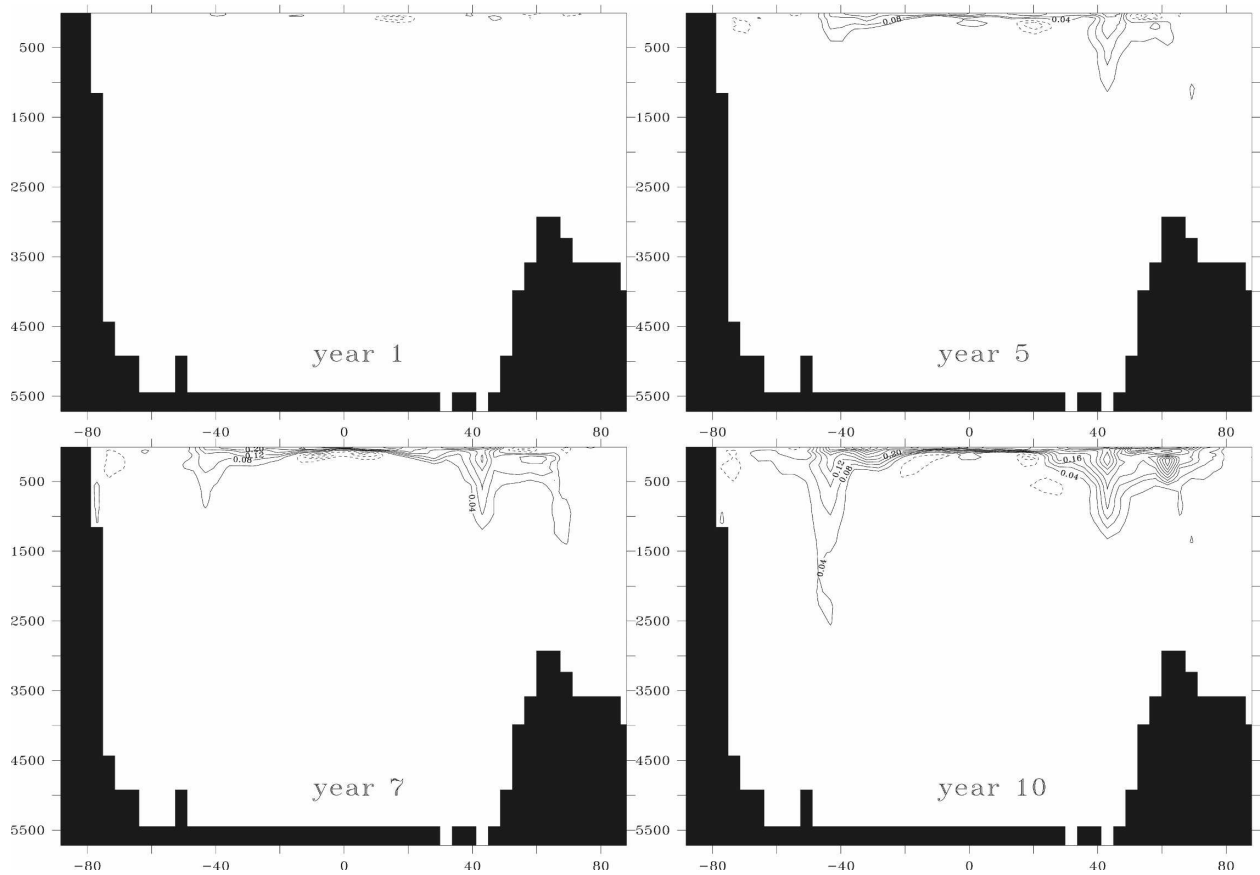
FIG. 15. Meridional and depth sections of ensemble mean difference in zonally averaged ocean temperature (C°) in year (top left) 1, (top right) 5, (bottom left) 7, and (bottom right) 10. The isoline interval is 0.04 C°. Solid (dashed) lines indicate positive (negative) values. Zero line is not plotted.

of the second kind can be notably enhanced if the external forcing persists and amplifies over lead time. Despite this favorable feature, predicting the coupled atmosphere–ocean system under a changing CO_2 forcing is far from being straightforward. One major obstacle is the lack of knowledge about the future evolution of CO_2 forcing, whose prediction requires modeling of interactions between economy and policy. Without a reliable prediction of the future CO_2 forcing, all predictions will be subject to, in addition to the perfect model assumption, the assumption about the possible future forcing changes. The problem could be particularly severe for a nonlinear system with multiple equilibriums. In this case, predictions could be distinctly different (i.e., they differ not only in amplitude but also in structure), depending on whether or not the forcing used can make the system to reach certain thresholds. For small forcing changes, on the other hand, the dependence of the responses on the detailed evolution of the forcing is expected to be weak. This paper provides a detailed analysis of the potential predictability subject to small-

amplitude forcing changes obtained after imposing the change over a short time period. The skill derived by utilizing such potential predictability is assessed by Lee et al. (2006). Further investigations are needed to quantify the difference between the short- and long-term responses.

The second obstacle is that an external forcing like that resulting from CO_2 concentration does not uniquely determine the climate state. Instead there are a large number of states, all of which are consistent with a given CO_2 concentration, implying a large uncertainty related to the forcing. This uncertainty can be quantified by the ensemble spread. When measuring the potential predictability by mean changes between prediction and reference ensemble, the utility of this predictability will be limited by the uncertainty resulting from ambiguous control of the external forcing. To take this explicitly into account, the present paper uses the signal-to-noise ratio, that is, the ratio of the magnitude of the mean ensemble difference to ensemble spread, as a measure to quantify the gain in the predictability re-
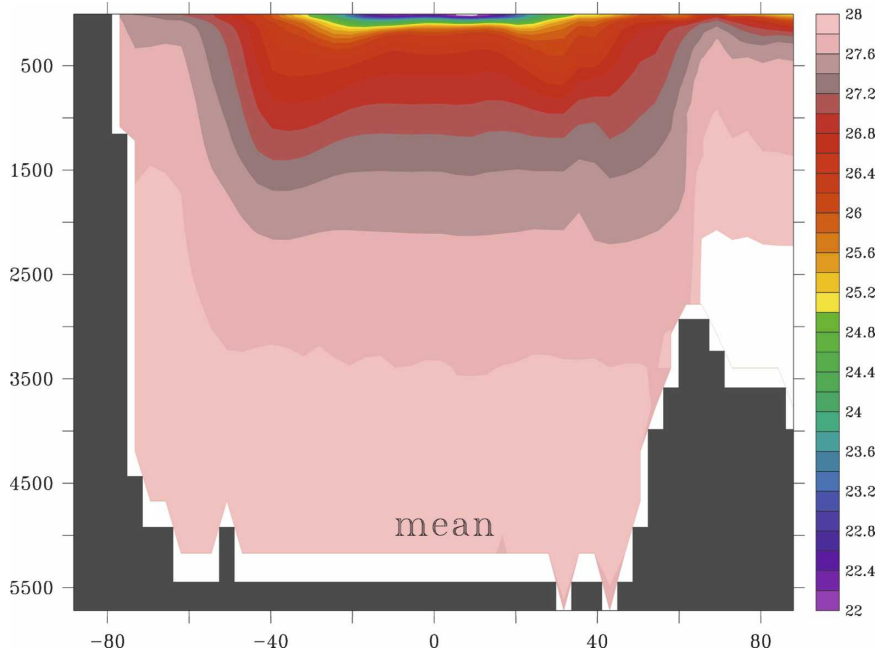
FIG. 16. Mean zonally averaged potential density as function of latitude and depth (m), as derived from the reference run. Plotted are potential density minus 1000 in kb/m^3

sulting from imposing CO_2 forcing. In general, probabilistic concepts are required to deal with these uncertainties.

b. First responses of the coupled system to an increase in CO_2 concentration

The origin of the potential predictability lies in the first responses, that is, responses obtained after the system is subjected to an increase in CO_2 forcing for a short time period. The responses describe how the coupled system is steered by the CO_2 forcing.

A forcing resulting from an increase in CO_2 concentration is a global-scale forcing according to the IPCC Fourth Assessment Report (see "Summary for Policymakers" online at http://www.ipcc.ch/) and can be considered as being homogeneously distributed. Nevertheless, the response of the coupled system to this forcing is highly nonhomogeneous and reveals strong spatial variations, particularly in the meridional direction. The main meridionally oriented responses are, in one way or another, related to the significant increase in meridional gradient of SST in the Southern Ocean. The increase in meridional temperature gradient results from a stronger warming in the subtropics relative to that near 55°–60°S. Related to the increase in the meridional temperature gradient are

- a strengthening of the Ferrel cell in the Southern Hemisphere,

- a strengthening of the vertically averaged zonal mean zonal winds over the Southern Ocean,
- an increase in zonal wind stress at the sea surface centered at about 55°S and a decrease centered at about 35°S,
- a strengthening of northward Ekman transport between 40° and 60°S and a strengthening of southward Ekman transport north of 40°S.

These features constitute the following positive feedback: The increase in temperature gradient changes the atmospheric circulation, leading to a stronger northward Ekman transport centered near 55°S. The latter transports cold Antarctic water northward and counteracts on the increased downward heat flux at about 55°S, thereby maintaining the temperature gradient. The strengthening of the Ferrel cell indicates that the feedback process is initialized by an increase in temperature gradient, which presumably results from the subtropical warming induced by the radiative forcing. The identified responses are not described by the long scenario runs of the IPCC Fourth Assessment Report, in which the high-latitude warming was identified as the main temperature signal. The positive feedback could affect the storms in the Southern Ocean. However, further analysis is required to clarify this issue.

The positive feedback, which is confined to the atmosphere and the upper ocean, controls only the horizontal distribution of heat. Below the first few hundred

meters of the ocean, the warming signal propagates downward through two corridors, one near 40°S and the other near 40°N, and reaches 1000–2500 m already in year 5. There is some evidence that the downward propagation of the warming signal is caused by the isoneutral mixing. Further studies are needed to verify this issue. The downward propagation of the warming signal effectively reduces the warming in the atmosphere and the upper ocean.

It should be stressed that the present study is based on the perfect model assumption. Because the extent to which the ocean model realistically represent mixing processes is still debatable, the way in which the warming signal is transported downward, and consequently the rate of the warming in the atmosphere and the upper ocean, may depend strongly on the parameterization implemented in the ocean model.

REFERENCES

Anderson, J. L., and W. F. Stern, 1996: Evaluating potential predictive utility of ensemble forecasts. *J. Climate,* **9,** 260–269.

Compo, G. P., and P. D. Sardeshmukh, 2004: Storm-track predictability on seasonal and decadal scales. *J. Climate,* **17,** 3701–3720.

Fyfe, J. C., and O. A. Saenko, 2006: Simulated changes in the extratropical Southern Hemisphere winds and currents. *Geophys. Res. Lett.,* **33,** L06701, doi:10.1029/2005GL025332.

Griffies, S. M., A. Gnanadesikan, R. C. Pacanowski, V. D. Larichev, J. K. Dukowicz, and R. D. Smith, 1998: Isoneutral diffusion in a z-coordinate ocean model. *J. Phys. Oceanogr.,* **28,** 805–830.

Hegerl, G. C., H. v. Storch, K. Hasselmann, B. D. Santer, U. Cubasch, and P. D. Jones, 1996: Detecting greenhouse gas induced climate change with an optimal fingerprint method. *J. Climate,* **9,** 2281–2306.

Jungclaus, J. H., H. Haak, M. Latif, and U. Mikolajewicz, 2005: Arctic–North Atlantic interactions and multidecadal variability of the meridional overturning circulation. *J. Climate,* **19,** 4016–4034.

——, and Coauthors, 2006: Ocean circulation and tropical variability in the coupled model ECHAM5/MPI-OM. *J. Climate,* **19,** 3952–3972.

Kleeman, R., 2002: Measuring dynamical prediction utility using relative entropy. *J. Atmos. Sci.,* **59,** 2057–2072.

Kumar, A., and M. P. Hoerling, 1998: Annual cycle of Pacific–North American seasonal predictability associated with different phases of ENSO. *J. Climate,* **11,** 3295–3308.

——, and ——, 2000: Analysis of a coupled model of seasonal climate variability and implications for seasonal prediction. *Bull. Amer. Meteor. Soc.,* **81,** 255–264.

Lee, T. C. K., F. W. Zwiers, X. Zhang, and M. Tsao, 2006: Evidence of decadal climate prediction skill resulting from changes in anthropogenic forcing. *J. Climate,* **19,** 5305–5318.

Marsland, S. J., H. Haak, J. H. Jungclaus, M. Latif, and F. Roeske, 2003: The Max-Planck-Institute global ocean/sea ice model with orthogonal curvilinear coordinates. *Ocean Modell.,* **5,** 91–127.

Meehl, G. A., and Coauthors, 2007: Global climate projections. *Climate Change 2007: The Physical Science Basis,* S. Solomon et al., Eds., Cambridge University Press, 749–844.

Murphy, J. M., 1988: The impact of ensemble forecasts on predictability. *Quart. J. Roy. Meteor. Soc.,* **114,** 89–125.

Redi, M. H., 1982: Oceanic isopycnal mixing by coordinate rotation. *J. Phys. Oceanogr.,* **12,** 1154–1158.

Roeckner, E., and Coauthors, 1998: Impacts of horizontal resolution on simulated climate statistics in ECHAM4. Max-Planck-Institut für Meteorologie Rep. 253, 57 pp.

——, and Coauthors, 2003: The atmospheric general circulation model ECHAM5, Part I: Model description. Max-Planck-Institut für Meteorologie Rep. 349, 127 pp.

Rowell, D. P., 1998: Assessing potential seasonal predictability with an ensemble of multidecadal GCM simulations. *J. Climate,* **11,** 109–120.

Sardeshmukh, P. D., G. P. Compo, and C. Penland, 2000: Changes of probability associated with El Niño. *J. Climate,* **13,** 4268–4286.

Schneider, T., and S. M. Griffies, 1999: A conceptual framework for predictability studies. *J. Climate,* **12,** 3133–3155.

Shin, S.-I., P. D. Sardeshmukh, R. S. Webb, R. J. Oglesby, and J. J. Barsugli, 2006: Understanding the Mid-Holocene climate. *J. Climate,* **19,** 2801–2817.

Shukla, J., 1981: Dynamical predictability of monthly means. *J. Atmos. Sci.,* **38,** 2547–2572.

Tippett, M. K., R. Kleeman, and Y. Tang, 2004: Measuring the potential utility of seasonal climate predictions. *Geophys. Res. Lett.,* **31,** L22201, doi:10.1029/2004GL021575.

von Storch, H., and F. Zwiers, 1999: *Statistical Analysis in Climate Research.* Cambridge University Press, 484 pp.

Zwiers, F. W., 1996: Interannual variability and predictability in an ensemble of AMIP climate simulations conducted with the CCC GCM2. *Climate Dyn.,* **12,** 825–847.

——, 2002: The 20-year forecast. *Nature,* **416,** 690–691.